Solar Physics (2006) 236: 75–95
DOI: 10.1007/s11207-006-0089-2

ELECTRON ACCELERATION AND TRANSPORT DURING THE NOVEMBER 5, 1998 SOLAR FLARE AT ∼13:34 UT

G. TROTTET
Observatoire de Paris, Section de Meudon, LESIA, F-92190, Meudon, France
(e-mail: gerard.trottet@obspm.fr)

E. CORREIA
INPE-CRAAM, Universidade Presbiteriana Mackenzie, Rua da Consolação, 896, 01302-907, São Paulo, SP, Brazil
(e-mail: ecorreia@craam.mackenzie.br)

M. KARLICKÝ
Astronomical Institute, Academy of Sciences of the Czech Republic, 251 65 Ondřejov, Czech Republic
(e-mail: karlicky@asu.cas.cz)

G. AULANIER
Observatoire de Paris, Section de Meudon, LESIA, F-92190, Meudon, France
(e-mail: guillaume.aulanier@obspm.fr)

Y. YAN
National Astronomical Observatories, Chinese Academy of Sciences, Beijing 100012, China
(e-mail: yyh@bao.ac.cn)

and

P. KAUFMANN
CRAAM, Universidade Presbiteriana Mackenzie, Rua da Consolação, 896, 01302-907, São Paulo, SP, Brazil
(e-mail: kaufmann@craam.mackenzie.br)

(Received 13 October 2005; accepted 27 December 2006)

Abstract. This paper deals with a detailed analysis of spectral and imaging observations of the November 5, 1998 (Hα 1B, GOES M1.5) flare obtained over a large spectral range, *i.e.*, from hard X-rays to radiometric wavelengths. These observations allowed us to probe electron acceleration and transport over a large range of altitudes that is to say within small-scale (a few 10^3 km) and large-scale (a few 10^5 km) magnetic structures. The observations combined with potential and linear force-free magnetic field extrapolations allow us to show that: (i) Flare energy release and electron acceleration are basically driven by loop–loop interactions at two independent, low lying, null points of the active region magnetic field; (ii) $<$300 keV hard X-ray-producing electrons are accelerated by a different process (probably DC field acceleration) than relativistic electrons that radiate the microwave emission; and (iii) although there is evidence that hard X-ray and decimetric/metric radio-emitting electrons are produced by the same accelerator, the present observations and analysis did not allow us to find a clear and direct magnetic connection between the hard X-ray emitting region and the radio-emitting sources in the middle corona.

1. Introduction

It is well documented that flare magnetic energy release is most often associated with more complex magnetic structures than a single bipolar configuration. Early evidence of this came from Solar Maximum Mission solar flare observations, which showed, that during the impulsive phase, strong electron acceleration and heating occurs in two or more magnetic structures. Since then, loop–loop interactions have been considered as a basic driver for triggering a flare. This has been further supported by joint observations in the X-ray and microwave domains (Hanaoka, 1997; Nishio *et al.*, 1997). Spectral measurements in the hard X-ray (HXR) domain combined with decimetric/metric (dm/m) radio-imaging observations have also shown that various small- and large-scale coronal structures are activated during a flare (*e.g.*, Trottet *et al.*, 1994). The spectral characteristics of the accelerated electrons, deduced from HXR observations, were found to evolve, during a given flare, in close temporal association with the activation of large-scale magnetic structures traced by radio emission (Raoult *et al.*, 1985; Chupp *et al.*, 1993; Trottet *et al.*, 1994, 1998). Moreover, the detection of fast time structures in the millimeter domain (Kaufmann *et al.*, 1980; Correia *et al.*, 1995; Raulin *et al.*, 1998) and in the HXR domain (Hurley *et al.*, 1983; Kiplinger *et al.*, 1983; Aschwanden, Schwartz, and Alt, 1995; Vilmer *et al.*, 1995), as well as evidence for their simultaneity in both domains (Kaufmann *et al.*, 2000), have shown that non-thermal energy release in flares may be the response of multiple discrete accelerations of non-thermal electrons, which occur on sub-second time scales. This is in line with radio millimeter observations of one flare, which show that the centroid of the positions of sub-second bursts at 48 GHz varied from a few to a few tens of arcseconds (Correia *et al.*, 1995; Raulin *et al.*, 1998). This suggests various episodes of electron acceleration at different places of the flaring magnetic structures. More recently, simultaneous imaging observations at soft X-ray (SXR), HXR, millimeter, and dm/m wavelengths showed that different episodes of energy release are triggered by loop–loop interaction and that the site of particle acceleration and/or injection changes rapidly inside the energy-release volume (Raulin *et al.*, 2000).

In this paper, we analyze spectral and imaging observations of the November 5, 1998 solar flare obtained simultaneously over a wide range of wavelengths, *i.e.*, from the X-ray domain to the dm/m radio domain. These data and extrapolations of the photospheric magnetic field are used to discuss the magnetic structure associated with the acceleration and transport of electrons up to relativistic energies.

2. Observations

The November 5, 1998 Hα 1B flare (GOES M1.5) occurred in NOAA region 8375 (N15 W17). The impulsive phase of this flare started at about 13:34 UT and

vanished at about 13:35:20 UT. It was observed from the HXR domain (energies above ∼20 keV) to the decametric radio domain. Figure 1a shows the event time profiles in four HXR energy bands and at selected microwave frequencies, overlaid on the dynamic radio spectrum observed, in the 800 – 4400 MHz frequency range, by the AO Ondřejov Spectrograph (time resolution 0.1 s). The HXR time profiles were obtained with the Burst and Transient Source Experiment (BATSE) on CGRO (Pendleton *et al*., 1996) with a time resolution of 1.024 s. The 7 GHz total flux density was provided by the 1.5 m dish Solar Radio Polarimeter operating at Itapetinga Radio Observatory with a time resolution of 60 ms and a sensitivity of ∼0.5 sfu, in both circular polarization modes (R and L). Total flux density measurements at 1.4, 2.7, 5.0, 8.8, and 15.4 GHz (1 s time resolution) from the Radio Solar Telescope Network (RSTN) have also been used. Similarly, Figure 1b displays the time evolution of the radio-flux densities at 164, 236, 327, 410, and 432 MHz overlaid on the radio-dynamic spectrum in the 60 – 800 MHz frequency range. It also shows the time evolution of the 25 – 50 keV HXR intensity for comparison. The total flux densities were computed from the 2D images recorded by the Nançay Radioheliograph (Kerdraon and Delouis, 1997), referred to below as NRH, at a rate of two images per second at each of the five observing frequencies. The radio-dynamic spectrum in the 60 – 800 MHz domain is from the radio spectrometer of Astrophysikalisches Institut Potsdam (courtesy of H. Aurass). Figure 1 shows:

(a) A gross similarity between time profiles at all wavelengths. In particular, the different emissions start and vanish simultaneously within 1 s or so.
(b) The HXR and microwave time profiles exhibit a slow rise (∼50 s) and fast decay (1/e decay time ∼3 s). They show stepwise increases at the beginning of each of the 20 s time intervals marked I, II, III, and IV in Figure 1 (see Section 2.1).
(c) In the dm/m domain, the emission (Figure 1b) started with weak short-lived bursts showing fast drifts towards lower frequencies that are characteristic of type III bursts. The start frequency of these type III or type III-like bursts is about 350 MHz (*e.g.*, burst at 13:34:05 UT). After 13:34:20 UT the radio emission consists of strong type III bursts superimposed on a wide-band continuum. The start frequency of type III's increases from 400 MHz (*e.g.*, burst at 13:34:26 UT) to >1500 MHz at the end of the event (13:34:57 – 13:35:13 UT). Furthermore, the burst structure is complex and exhibits different fast-frequency drifts at 13:34:46 – 13:34:52 UT in the 270 – 370 MHz frequency range and type U bursts at 13:34:59 – 13:35:02 and 13:35:14 – 13:35:16 UT in the 220 – 250 MHz range. This suggests that electron beam trajectories change with time.

Although it cannot be clearly seen in Figure 1, a detailed examination of the radio-dynamic spectra between 300 and 4400 MHz reveals the occurrence of a few pairs of type III and reverse slope (RS) bursts. RS are short-lived bursts, which drift

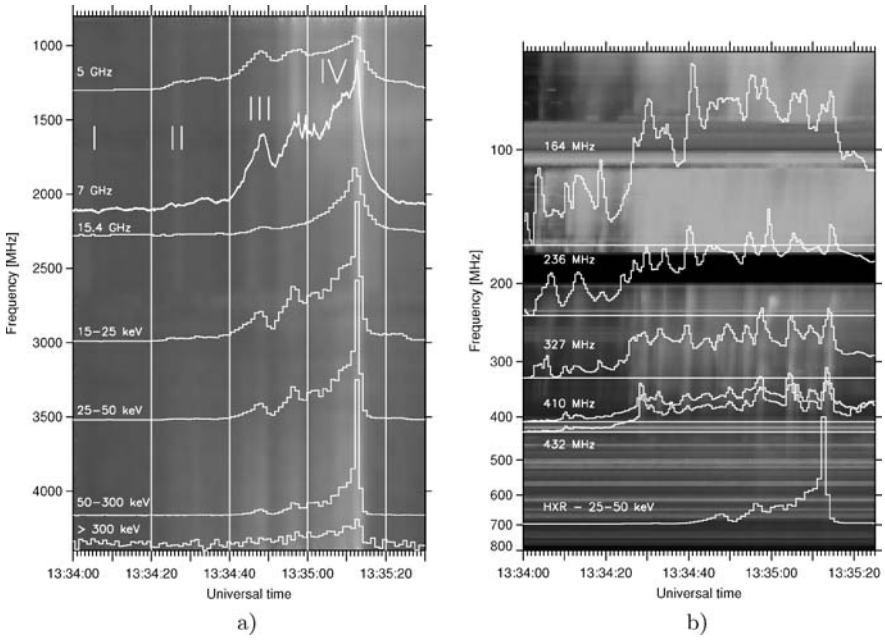

Figure 1. Time evolution of the November 5, 1998 flare: (a) Time histories of the normalized flux densities at 5, 7, and 15.4 GHz and HXR time profiles in four energy bands (normalized scale) plotted over the radio-dynamic spectrum in the 0.8 – 4.4 GHz band; (b) Time profiles of the radio-flux density at the five NRH frequencies (normalized logarithmic scale) plotted over the radio-dynamic spectrum in the 40 – 800 MHz band. The time behavior of the 25 – 50 keV HXR emission is also shown for comparison.

towards higher frequencies. These pairs of III and RS bursts start simultaneously at about the same frequency, which, like the start frequency of type III's, also shifts towards higher frequencies as the event progresses, namely from 327 to 410 MHz at the beginning of the event (*e.g.*, burst at 13:34:28 UT) up to 3000 to 3600 MHz at 13:35:01 UT. For this latter burst, the frequency drift rates are ~ -3000 MHz s^{-1} and 2000 MHz s^{-1} for the type III and RS bursts, respectively. Such high drift rates are consistent with those reported by, *e.g.*, Aschwanden, Benz, and Schwartz (1993) in this frequency range. There is also a RS burst between 13:34:52 and 13:34:53 UT in the 3700 – 4400 GHz range with a similar frequency drift rate. For the other fast drift bursts observed in the 800 – 4400 MHz domain, in particular at 13:35:12 UT (maximum of the HXR emission), the time resolution of the spectral data (0.1 s) is not sufficient to estimate the frequency drift rate. It is well documented that type III and RS bursts are signatures of electron beams, which propagate upward and downward through the solar atmosphere, respectively.

2.1. Microwave and HXR emissions

The slow increase of the microwave (frequencies above 2 GHz) and HXR emission shows successive groups of bursts with increasing flux densities, which correspond

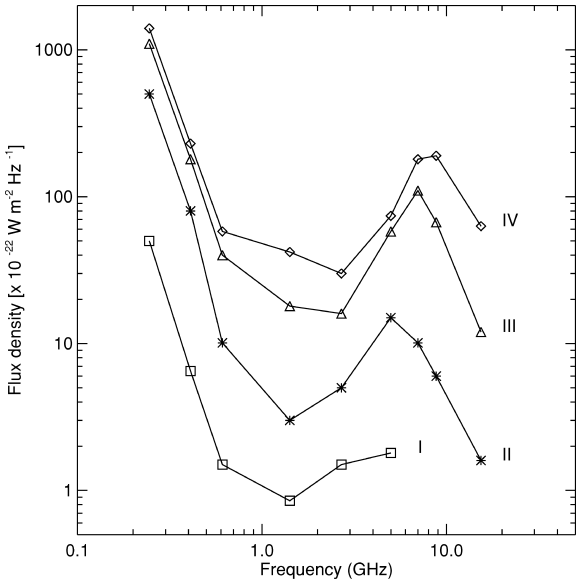

Figure 2. Mean radio spectra for the four intervals of time defined in Figure 1a.

to stepwise changes of the characteristics of the microwave emission. Early in the event (13:34:00 – 13:34:20 UT, interval I), the small flux densities shown in Figure 2 are within the pre-event background fluctuations so that there is no significant flare emission at frequencies above ∼1 GHz. After 13:34:20 UT, the microwave emission between 1.4 and 15.4 GHz comprises a slowly varying component whose spectrum is characteristic of gyrosynchrotron emission. Figure 2 shows that the turnover frequency of the gyrosynchrotron component increases by steps: ∼5 GHz from 13:34:20 to 13:34:40 UT (interval II), ∼7 GHz from 13:34:40 to 13:35:00 UT (interval III), and between 8.8 and 15.4 GHz from 13:35:00 to 13:35:20 UT (interval IV). Although the microwave emission is dominated by the gyrosynchrotron component, it comprises, as mentioned earlier, an additional component consisting of fast-drifting and short-lived type III and RS bursts some of them being observed up to 7 GHz. Figure 3 shows the time behavior of the right- and left-handed flux densities at 7 GHz. The slowly varying gyrosynchrotron emission is right-hand polarized, and its polarization degree decreases with time: ∼30% from 13:34:30 to 13:34:40 UT, ∼20% from 13:34:40 to 13:34:57 UT, and ∼10 % till the end of the impulsive phase at 13:35:20 UT. In contrast, there are two fast bursts at 13:34:57 and 13:34:59 UT, which are observed only in the left-handed flux density. There are no visible signatures of these, rather weak, bursts either in the 0.8 – 4.4 GHz dynamic spectrum or in the RSTN data at 5 and 8.8 GHz. This suggests that the two left-hand polarized bursts at 7 GHz are rather narrow band bursts. In summary, in the 1.4 – 7 GHz frequency range, the microwave emission comprises a wide-band

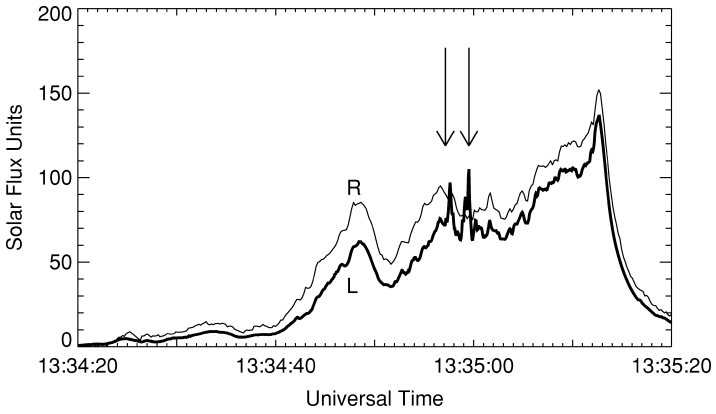

Figure 3. Time profiles of the November 5, 1998 flare at 7 GHz in R (*thin line*) and L (*thick line*) circular polarization modes.

gyrosynchrotron continuum emission and short bursts of small bandwidth emitted by collective plasma processes (see Figures 1 – 3).

The time evolution of the HXR emission is similar to that of the microwaves and exhibits groups of bursts with increasing intensities from interval I to interval IV (see Figure 1). The onset of the HXR emission seems to occur later with increasing energy. Indeed, the onset time of the HXR emission, taken as the instant where the number of excess counts is larger than 3σ, is found to be: 13:34:15 UT, 13:34:24 UT, 13:34:43 UT, and 13:35:00 UT for the 15 – 25, 25 – 50, 50 – 300, and >300 keV energy bands, respectively. These delays in the HXR onset times most likely result from the combined effect of the slow rise of the HXR emission and the decrease of the detector efficiency with increasing energies. It should be noted that, within the time resolution of the HXR measurements (1 s), there are no significant time delays either between the HXR peaks in different energy channels or between the HXR and microwave peaks (see Figure 1a).

2.2. HXR SPECTRAL ANALYSIS

BATSE spectral data consist in 16-channel count spectra, accumulated over 2.048 s, which cover the $\sim$20 – 2000 keV energy range (Pendleton *et al.*, 1996). From 13:34:45 UT (about the onset of >50 keV HXR emission) till 13:35:15 UT each measured spectrum could be reasonably well represented by a broken power-law in energy defined by the photon flux at 50 keV $A_{\rm ph}$, the break energy $E_{\rm b}$, the power law indices γ_1 and γ_2 below and above $E_{\rm b}$, respectively. The spectral fit was done from 25 keV up to the last energy channel where the count rate is 3σ above the background. Figure 4 shows the time evolution of the background-subtracted count rate in the 74 – 99 keV channel and of $E_{\rm b}$, γ_1 and γ_2. While $E_{\rm b}$ $\sim$50 – 60 keV does not vary much during interval III, it jumps to $\sim$100 keV near the beginning of in-

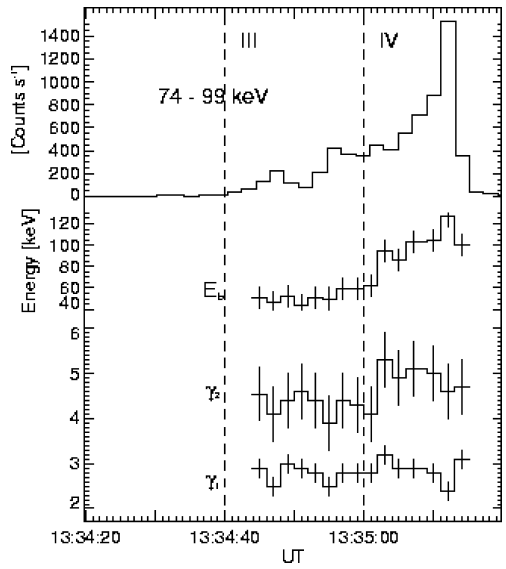

Figure 4. From *top* to *bottom*: Time evolution of the 74 – 99 keV BATSE rate (background subtracted), the spectral energy break E_b, and power law indices γ_2 and γ_1. III and IV refer to the intervals of time marked in Figure 1a.

terval IV. γ_1 remains nearly constant. The evolution of γ_2 indicates that above E_b the HXR spectrum becomes softer during interval IV.

2.3. HXR IMAGING

Observations of the Hard X-ray Telescope (HXT) on board Yohkoh (Kosugi *et al.*, 1991) provide the spatial distribution of the HXR emission in four energy bands referred to below as L (14 – 23 keV), Ml (23 – 33 keV), M2 (33 – 53 keV), and H (53 – 93 keV). The spatial resolution of the HXR images is $\sim 5''$. Figure 5 shows HXR maps accumulated over each of the four time intervals (20 s) defined above (from left to right), and for each of the four HXT energy bands (from top to bottom). The bottom panel of the figure displays the HXR time profile in the L-band. When the statistics was sufficient maps accumulated over 2 s have also been computed. Images in the L-band indicate that the HXR emission started during interval I within a single and rather compact ($\sim 10'' \times 10''$) source marked A on the figure. A new HXR-emitting source B, located north-east of A, appeared during interval II and both sources remained visible till the end of the HXR emission. Due to the motion of source B during interval IV (see later), its mean position during this interval is slightly different from its mean position during intervals II and III. More precisely, Figure 5 and the images obtained with a higher time resolution (2 s) show the following:

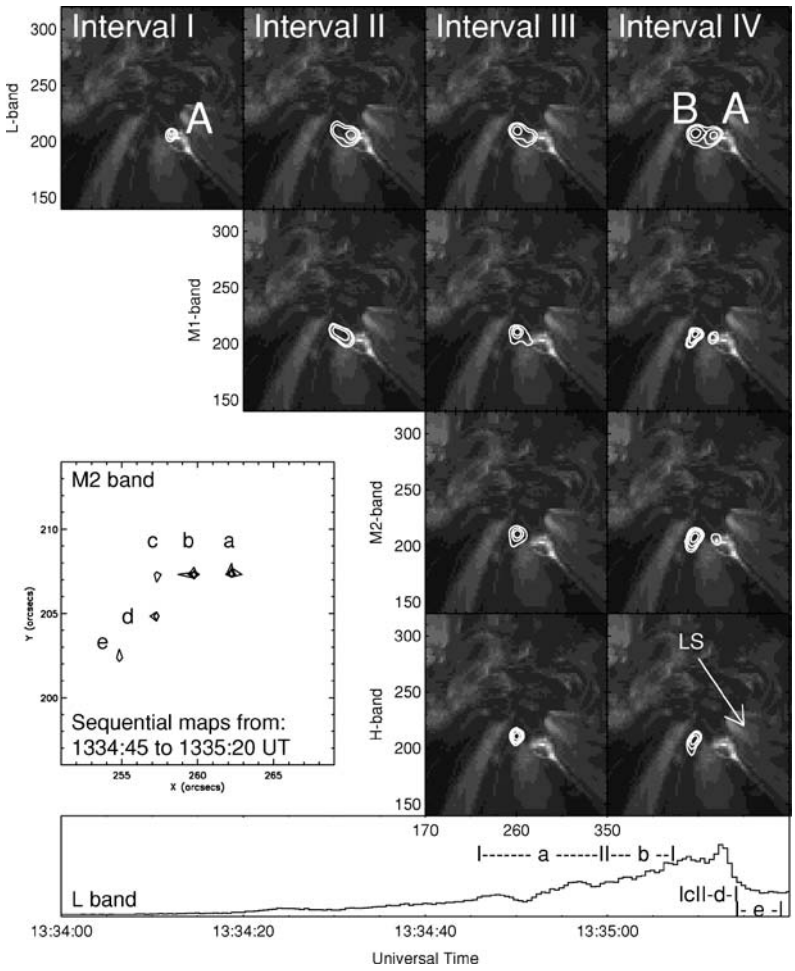

Figure 5. HXR images (*contours*) integrated over each of the four intervals of time marked in Figure 1a for each of the four HXT energy bands (L, M1, M2, H from *top* to *bottom*). They are overlaid on the 17.1 nm TRACE image obtained at 13:34:13 UT with an FOV of 3′ by 3′ centered on AR8375. A and B refer to the two HXR-emitting sources (see text). The HXR time profile in the L-band (14 – 23 keV) is displayed for reference at the *bottom* of the figure. The displacements of the centroid of source B in the M2-band are shown in the *lower-left side* of the figure for time intervals a to e, which are indicated in the HXR time profile. LS refers to the portion of the EIT large-scale loop system (see Figure 6) observed by TRACE.

(a) *Interval I*: Source A starts to be visible, in L-band only, after ∼13:34:15 UT, *i.e.*, near the end of this interval. This is in agreement with the onset time of the 15 – 25 keV HXR emission seen by BATSE.
(b) *Interval II*: A new source B appeared at the beginning of this time interval (13:34:20 UT) in the L-band. The ratio R of the maximum intensity of

source B to the maximum intensity of source A is ∼0.45. The 2 s images indicate that A and B start to be visible at ∼13:34:34 UT in the M1-band. After 13:34:38 UT, B is the brightest source in both L (R ∼1.3) and Ml (R ∼3).

(c) *Interval III*: Both A and B are visible in the L-band and B is brighter (R ∼3). In the M2-band, B appears at the beginning of this time interval (13:34:40 UT) and 6 s later in the H-band. Source A is not detected in the M1-, M2-, and H-bands, within the intrinsic dynamic range (10:1) of the HXT images.

(d) *Interval IV*: Source B is visible in all bands. Within the dynamic range of HXT images A is not detected in the H-band. For the L-, M1-, and M2-bands, R is respectively, ∼1.4, 8, and 8.

In Figure 5, the box labeled Sequential maps, displays the positions (a, b, c, d, and e) of the maximum of source B in the M2-band obtained from the 2 s maps computed between 13:34:45 and 13:35:20 UT. It shows that B jumps eastward from a to b at 13:35 UT (beginning of interval IV) and from b to c at 13:35:08 UT and then southward from c to d at 13:35:10 UT (maximum of the HXR emission) and from d to e at 13:35:14 UT (decay of the HXR peak). Although each jump of the position from a to e is small: ∼1 pixel (2.5″ × 2.5″), it seems to be significant because: (i) Similar displacements of the source maximum are seen in the four energy bands and, (ii) in the L-band, where both sources are visible with a 2 s accumulation time, source A does not show similar displacements: it just jumps ∼3″ westward (opposite to source B) and ∼5″ northward at the beginning of interval IV (13:35 UT). Within the spatial (5″) and time (2 s) resolution of the HXT maps it is not possible to determine whether the overall displacement of source B results from successive and discrete jumps of its position or from a continuous motion. Taking 2.5″ (the pixel size of HXR images) as the uncertainty on the position of an HXR source, the latter case would imply projected velocities of 1(300 ± 140) km s^{-1} toward east between 13:34:58 and 13:35:10 UT and (550 ± 300) km s^{-1} toward south between 13:35:10 and 13:35:16 UT. These velocities are in the range (∼50 – 500 km s^{-1}) of those measured by Fletcher and Hudson (2002) for flares of GOES class M4 and above.

2.4. DECIMETRIC/METRIC IMAGING OBSERVATIONS

The spatial distribution of the radio-emitting sources observed by the NRH has been examined for each of the short-lived bursts visible on the radio-dynamic spectrum displayed on Figure 1b. Using measurements of calibration sources made before and after the studied flare, we estimate that the accuracy of the absolute position of a given source is no better than 1′ at all observing frequencies. Figure 6 shows the radio source patterns observed for two bursts that occurred at 13:34:39

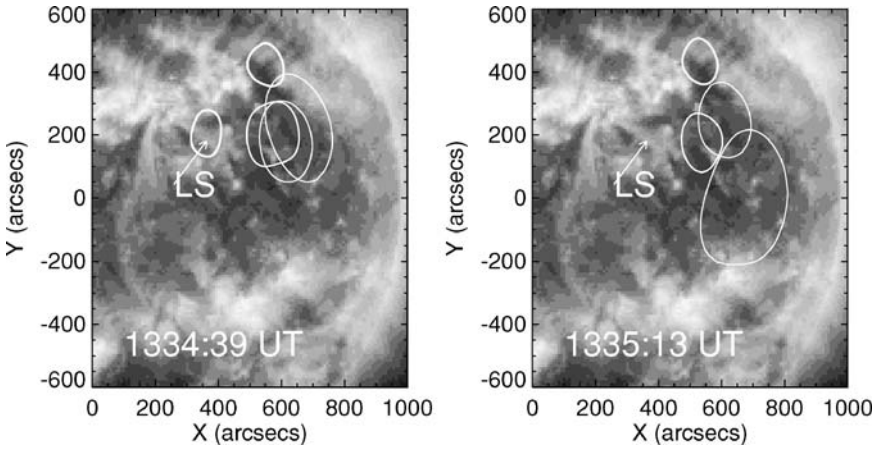

Figure 6. Typical pattern of the bursts observed by the NRH at 410, 327, 236, and 164 MHz before 13:34:53 UT (*left*) and after 13:34:53 UT (*right*) overlaid on the 19.5 nm EIT image taken at 13:24:34 UT. For each frequency, the contour level corresponds to 70% of the maximum brightness of the image (410, 327, 236, 164 MHz in the order of increasing size and decreasing thickness). LS refers to a large-scale loop system seen by EIT (see text).

UT (pattern I) and 13:35:13 UT (pattern II). The radio sources are overlaid on a 19.5 nm EIT image taken at 13:24:34 UT (the closest image to the flare). Since the positions of the 432 and 410 MHz sources are nearly coincident, the former is not shown in the figure. Briefly stated, patterns I and II represent the typical spatial distribution of the radio sources associated with bursts occurring respectively before (intervals I, II, and III) and after (interval IV) ∼13:34:53 UT, although the source position at a given frequency changes from burst to burst. This confirms the earlier suggestion from the spectrograph data that electron beam trajectories change with time. Despite these changes, pattern I is characteristic of type III electron beams with projected trajectories going westward from the flaring region. For pattern I, the projections of the 410 and 432 MHz radio-emitting sources lay above a bright-loop system marked LS on the EIT (Figure 6) and TRACE (Figure 5) maps. It should be noted that the HXR source A is located close to the base of the southern edge of LS. Besides the sources belonging to pattern I, Figure 6a also shows a 410 (432) MHz source located ∼4′ north and ∼3′ west of the flaring site. This source is not visible at lower frequencies and appeared sporadically during interval III. Pattern II is quite different from pattern I: (i) At 410 (432) MHz only the isolated source mentioned earlier is present and, (ii) the sources at frequencies $\leq$327 MHz are roughly aligned along the north–south direction. A careful examination of the radio spectrum reveals that although the short-lived bursts corresponding to pattern II drift globally towards low frequencies, these drifts are not continuous: The emission fades and starts again ∼0.5 s later between 350 and 380 MHz and between 250 and 270 MHz.

3. Discussion

The observations analyzed in the previous section provide spectral and spatial information on the radiative signatures of flare accelerated electrons over a wide range of altitudes going from the upper chromosphere/low corona (HXR, microwaves, short-decimeter waves) up to the middle corona (meter waves). These observations show globally the following:

(a) Although the radiative signatures of non-thermal electrons arise from sources spread over a wide altitudinal range and are emitted by different processes (bremsstrahlung and gyrosynchrotron emission for HXR and microwave radiation, respectively, collective plasma processes for dm/m waves), their time evolutions show a global and close similarity. Indeed they start and vanish nearly simultaneously and there is a close association of some HXR peaks (*e.g.*, 13:34:48 and 13:35:12 UT) with fast-drifting radio bursts seen from a few GHz down to 160 MHz (see Figure 1). In agreement with the findings of previous multi-wavelength studies of both moderate (Raulin *et al.*, 2000) and strong HXR events (*e.g.*, Raoult *et al.*, 1985; Chupp *et al.*, 1993; Trottet *et al.*, 1994), this provides strong indications that HXR- and radio-producing electrons are injected simultaneously in both small-scale ($10^3 - 10^4$ km) and large-scale (few 10^5 km) magnetic structures.

(b) The lack of significant delays exceeding 1 s (the time resolution of the HXR observations) between the HXR emission at different energies and between HXR and microwaves indicates that partial coronal trapping of electrons, if any, is not dominated by Coulomb collisions. This is further supported by the fact that HXR and microwaves show similar fast decay times after the event maximum (Figure 1). Thus, the HXR time history mostly reflects that of electron injection from the acceleration region(s). Under these conditions, intervals I to IV, correspond to successive episodes of electron acceleration resulting in stepwise changes of the characteristics of some of the electron radiative signatures observed near the transition from one interval to the subsequent one. These include: The increase of the start frequency of type III bursts and pairs of type III and RS bursts, the occurrence, at the transition from interval III to IV, of two bursts at 7 GHz with a sense of polarization opposite to that of the gyrosynchrotron emission (Figure 3), the appearance of a new HXR-emitting source during interval II (Figure 5), the increase by steps of the turnover frequency of the microwave gyrosynchrotron spectrum from 5 GHz during interval II to 8.8 – 15.4 GHz during interval IV (Figure 2) and the sudden jump of the HXR spectral break energy E_b from $\sim$50 keV during interval III to $\sim$100 keV and more during interval IV (Figure 4). The growth of the HXR emission and of E_b indicates that the efficiency of the acceleration process increases from interval I to interval IV.

3.1. DYNAMICS OF ACCELERATION

It is generally believed that the start frequency of pairs of type III and RS bursts corresponds to plasma frequencies and thus to densities in the acceleration region (*cf.* Bastian, Benz, and Gary, 1998; Aschwanden, 2001 and references therein). In the present event, this start frequency increases from 300 to 400 MHz at the beginning of interval II to 3 to 3.6 GHz at the beginning of interval IV. This indicates that the density in the acceleration region increases from $2(0.5) \times 10^9\,\mathrm{cm}^{-3}$ to $1.5(0.4) \times 10^{11}\,\mathrm{cm}^{-3}$ for fundamental (harmonic) emission. This may reflect changes of the location of the electron acceleration/injection or/and a density increase. Its cause may either be attributed to chromospheric evaporation or to the change of altitude of the null points as expected during magnetic reconnection. It should be remarked that this density increase is associated with that of acceleration efficiency.

While during interval I the HXR emission comes from source A, visible only in the L-band, during interval II a new HXR source B appeared and was observed in both the L- and M1-bands. In order to identify the magnetic structure associated with the HXR-emitting regions the photospheric magnetic field has been extrapolated in a large region of $\sim 13' \times 13'$ centered on the HXR-emitting region. The extrapolation was performed with 512×512 points in the horizontal direction, using the code developed by Démoulin *et al*. (1997) in the frame of a request which we did on the FRench Online MAGnetic Extrapolation (FROMAGE) web interface. The photospheric magnetic field was obtained from a full-Sun map recorded by the MDI instrument on SOHO at 12:48:04 UT, *i.e.*, 46 min before the flare onset. Only a sub-region of $\sim 8' \times 6'$ of the full disc magnetogram was used for the extrapolation. Although electric currents play a major role during flares, we use only potential field extrapolations because the overall topology of the magnetic field tends not to be qualitatively modified if the currents are neither too strong nor too extended beyond the size of the full region. This seems to be the case here since no XUV sigmoïd was observed. Figure 7 shows selected field lines connected with sources A and B, superimposed on the MDI magnetic field map. It shows that A and B are located in two independent loop systems, which connect small negative polarities to the main active region positive polarity. RA and RB show the positions of null points between the small-loop systems associated with the HXR sources and the more extended ones shown in the figure. Therefore, RA and RB appear as possible places for magnetic reconnection due to loop–loop interaction (Priest and Forbes, 2000) giving rise to energy release and acceleration of HXR and radio-emitting electrons. The transition from interval I to II thus corresponds to the appearance of a new region of electron acceleration (RB). This new acceleration region produced more energetic electrons, since the HXR source B is brighter and observed up to higher photon energies than source A (see Figure 5). Huang and Ji (2005) also reported the presence of two separate energy-release sites for a flare of similar GOES class (M2.0) as the November 5, 1998 event. For the present flare, it should

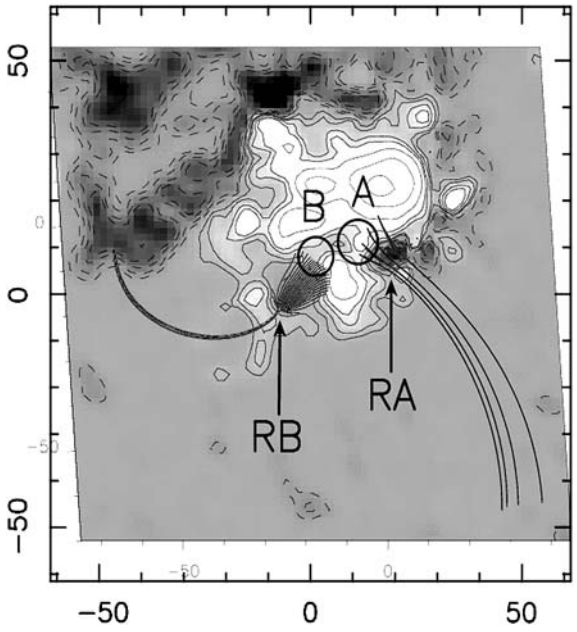

Figure 7. Partial field of the view of the potential field extrapolation in the vicinity of the X-ray sources A and B (*circles*, see also Figure 5). The *grey scale image* is the SOHO/MDI photospheric magnetic field. RA and RB designate low-altitude null points. The drawn magnetic field lines (*solid lines*) are those located close to the separatrices of RA and RB. Spatial units are arcsec.

be noted that there is no observational evidence for a causal relationship between RA and RB.

The transition from interval III to IV is associated with the occurrence of two highly polarized narrowband 7 GHz bursts. These rapidly varying bursts and the continuum microwave emission (gyrosynchrotron radiation) are polarized in the opposite sense. This strongly suggests that these two 7 GHz bursts are radiated by fundamental plasma emission in the o-mode, implying a density of $\sim 6 \times 10^{11}$ cm^{-3} in radio-emitting region. Due to the high opacity in such a dense plasma, a large inhomogeneity in density is needed to allow the 7 GHz emission to escape. Although harmonic radio emission radiated by nonlinear conversion processes has been occasionally observed up to 11.8 GHz (Stähli, Magun, and Shanda, 1987), it may be the first time that fundamental emission is detected at such a high frequency. Because these two 7 GHz bursts are not observed at other frequencies, the present observations do not allow us to specify their spectral characteristics. A plausible, but not unique, scenario is that these bursts are the signature of some explosive phenomenon that initiates the eastward motion of the hard X-ray source B and the sudden change of the dm/m emission pattern.

It should be noted that the displacement of source B occurs in association with: (i) A strong HXR flux increase with significant counts up to >300 keV, (ii) the jump

of E_b to $\sim$100 keV, and (iii) the shift of the gyrosynchrotron turnover frequency from 5 to 8.8 – 15.4 GHz. Moreover, the speed of source B displacement increases during the HXR maximum. Similar behavior of HXR sources has been reported for several flares by, *e.g.*, Krucker, Hurford, and Lin (2003), Fletcher and Hudson (2002) and Qiu *et al*. (2002). They have been taken as an evidence for an increase of the reconnection rate and thus an increase of the acceleration efficiency during flares. Assuming that the measured X-ray source velocity is predominantly perpendicular to the flare ribbon, if B_n is the magnetic field normal to the ribbon, the electric field E at the null point is given by $E_c = vB_n$ (*e.g.*, Priest and Forbes, 2000). For $B_n \approx 600$ G and using the velocities of HXR source B given in Section 2.3, we obtained $E_c \sim (180 \pm 90)$ V cm^{-1} and $\sim(330 \pm 180)$ V cm^{-1} for the eastward and southward displacements, respectively. These values of E_c are somewhat larger than, but of the same order of magnitude as the maximum value, 90 V cm^{-1}, obtained by Qiu *et al*. (2002) for a similar value of B_n. They are also much larger than the Dreicer field (Dreicer, 1959), $\sim 10^{-5}$ V cm^{-1}, expected in the corona (*e.g.*, Holman, 1985). For the present flare, electron acceleration should thus have occurred in the super-Dreicer regime.

The stepwise (quasi-periodic) nature of the event in the times intervals II – IV resembles types of flares reported by, *e.g.*, Tajima *et al*. (1987), Kundu *et al*. (2001), and Fárník, Karlický, and Švestka (2003) that show pulsations with periods ranging from about 5 to 50 s in the rising phase of or during microwave and HXR bursts. Several models have been proposed to explain this quasi-periodic behavior including interaction between current carrying loops (Tajima *et al*., 1987; Sakai and de Jager, 1996) and modulation of the non-thermal population of electrons as a result of MHD oscillations of the flaring loops (*e.g.*, Trottet, Pick, and Heyvaerts, 1979; Roberts, Edwin, and Benz, 1984; Aschwanden, 1987; Kundu *et al*., 2001).

3.2. Energetics of accelerated electrons

From 13:34:45 to 13:35:15 UT, the HXR spectrum is well represented by a broken power law (see Figure 4) with $E_b \sim 50 – 100$ keV, the spectrum being steeper above E_b. Such a spectral shape has been reported for numerous HXR bursts detected with energy resolution similar to that of BATSE (*e.g.*, Kane, Benz, and Treumann, 1982; Dulk, Kiplinger, and Winglee, 1992). A similar spectral shape was also derived from measurements with higher ($\sim$1 keV) energy resolution (Lin and Schwartz, 1987; Brown and Kontar, 2005 and references therein). Note that a discontinuous downward knee in the photon spectrum does not correspond to a sharp knee in the electron energy spectrum but to an upward step (Brown *et al*., 1991). HXR downward knees have been taken as an indication of DC electric field acceleration (*e.g.*, Lin and Schwartz, 1987; Dulk, Kiplinger, and Winglee, 1992). For $E_b \sim$ 100 keV, the DC electric field has a potential drop of $\sim$100 – 150 keV. Such an interpretation is consistent with the present observations which suggest that electron

acceleration is the consequence of magnetic reconnection at RA and RB (see Figure 7). It should be pointed out that, given the electric field strength derived above ($\sim$200 V cm^{-1}), the acceleration of electrons up to 100 keV requires an effective acceleration length of a few meters. This is orders of magnitude smaller than the typical size of flaring active regions. A solution to this paradox was pointed out some time ago by Martens (1988) and later on by Litvinenko (1996). Indeed, due to the presence of a transverse magnetic field component in the reconnection region, particles escape quickly from the reconnecting current sheet. Thus, the actual acceleration length is several orders of magnitude smaller than that of the reconnecting current sheet.

We have to caution that the spectral resolution of BATSE data is not sufficient to constrain the shape of the HXR spectrum. Other spectral fits, such as a power law with an upper cut-off or roll over or a modified Bessel function, would also be acceptable. In any case the data show that the HXR spectrum, and thus the electron spectrum, deviates from a single power law. The HXR spectrum expected from thick-target interactions of electrons with a broken power law spectrum has been computed over two intervals of 4 s centered at 13:34:57 UT (HXR maximum during interval III) and 13:35:11 UT (maximum of the HXR burst during interval IV). The free parameters, A_e, the electron flux at 1 keV, ϵ_b the break energy, δ_{X1} and δ_{X2} the power law indices below and above ϵ_b, respectively, are obtained by fitting the expected HXR spectrum to the observed one. The values of δ_{X1}, δ_{X2}, and ϵ_b are found to be respectively $\sim$4.2, 6.2, and 150 keV at 13:34:5.7 UT and 3.4, 6.2, and 300 keV at 13:35:11 UT. For these parameters, the energy deposition rate above 25 keV in the HXR-emitting region is $\sim 2 \times 10^{27}$ erg s^{-1} at 13:34:57 UT and $\sim 3 \times 10^{27}$ erg s^{-1} at the event maximum. This corresponds to a HXR event of moderate size (Crosby, Aschwanden, and Dennis, 1993). Hard HXR, *i.e.*, electron spectra below, a cut-off energy (see Figure 4) are broadly consistent with the expectations of charged particle orbit calculations in the framework of magnetic reconnection models (see Wood and Neukirch, 2005 and references therein for details). However, the present values of electron spectral indices cannot be strictly compared to those expected from these theories. Indeed, numerical simulations do not include energy losses and refer to particle spectra in the acceleration region while observations refer to the spectrum of interacting particles producing the HXR emission at location(s) most likely remote from the acceleration region(s).

As noted above, electron trapping plays a minor role in this event. It is thus reasonable to assume that electrons stream freely along the magnetic field and produce microwaves by gyrosynchrotron emission in the low corona and HXR by thick-target interactions in the chromosphere. The spectral index δ_R of the slope of the instantaneous spectrum of microwave radiating electrons is given by $\delta_R \approx \delta_X + 0.5$ and $\delta_R \approx \delta_X$ for electrons below and above $\approx$ 100 keV (*e.g.*, Trottet *et al.*, 1998). Using this and the parameters obtained above for the spectrum of HXR-producing electrons, the microwave spectrum was computed for a homogenous magnetic field using the code described in Holman (2003). The computed

spectrum depends on various parameters, such as source size and ambient density, magnetic field strength, which are not constrained by the present data. However, the slope α of the optically thin part of the spectrum is almost independent of these parameters and mostly depends of the slope of the spectrum of the radiating electrons (*e.g.*, Ramaty, 1969; Dulk and Marsh, 1982; Klein and Trottet, 1984). The values of α obtained from the electron spectra estimated above at 13:34:57 and 13:35:11 UT are respectively ~ -6 and ~ -4.5. These values of α are substantially larger than those, ~ -3 and ~ -1.9, obtained from the observations. This indicates that the microwave spectrum above the turnover frequency (7 and 8.8 GHz, respectively) is radiated by high-energy electrons (say, above a few hundreds of keV) with a harder spectrum than that of HXR-emitting electrons. This is consistent with earlier observations of weak (Kundu *et al*., 1994) and strong (Trottet *et al*., 1998, 2000) radio millimeter/centimeter-events. The bremsstrahlung continuum from this hard population of electrons is not detected within the sensitivity of BATSE. This suggests that the bulk of HXR-producing electrons and microwave-emitting electrons are accelerated by different mechanisms as, *e.g.*, DC electric field for electrons below ~300 keV and stochastic acceleration for higher energy electrons.

3.3. Large-scale magnetic field structure and dm/m type III burst sources

In Section 3.1, we argued that HXR-producing electrons are most probably accelerated at RA and RB. The close similarity between the time evolution of HXR and dm/m emissions would thus imply that dm/m-emitting sources are magnetically connected to RA and RB. However, there is no indication of such large-scale magnetic pattern in the available EIT images at 19.5 nm. The full-disc image of the photospheric magnetic field obtained with MDI at 12:48 UT was inserted into the synoptic magnetogram to serve as the boundary condition over the whole disk and the coronal field was reconstructed with the use of a potential extrapolation code that takes into account spherical geometry (Wang *et al*., 2002; Yan, 2005). Figure 8 displaysthe results for selected open- and closed-field lines. It shows that the radio sources are located in diverging fan-like (open) magnetic field structures. However, these open field lines (Figure 8a and b) do not show any direct magnetic connection between the radio sources observed for patterns I and II and the HXR sources A and B. The cartesian code used in Section 3.1 allows us to include electric currents in the linear force-free field approximation. We have performed such extrapolations for various values of the force-free parameter in order to search for a possible connection between the radio and HXR sources in the non-potential case. Those extrapolations did not result in finding such connections. This may suggest the presence of localized currents that would lead to different connectivities of the large-scale magnetic field than those revealed by potential or linear force-free

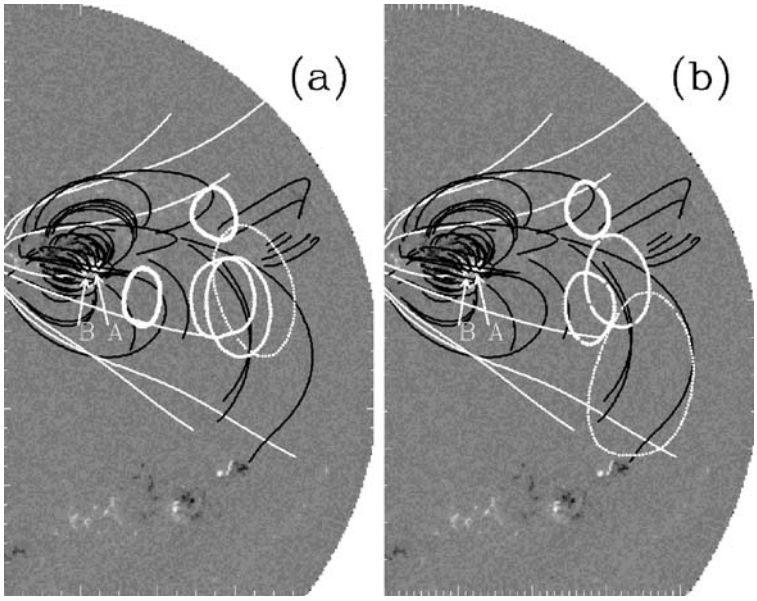

Figure 8. (a) Some selected open (*solid white*) and closed (*solid black*) field lines overlaid on the line of sight magnetogram (*greyscale with black/white* = ±600 G) taken at 12:48 UT by SOHO/MDI. Patterns of radio bursts by the NHR at 410, 327, 236, and 164 MHz at 13:34 UT (pattern I) are also displayed by contours, at 70% of the maximum brightness of the radio image, in an order similar to that in Figure 6. (b) The same as (a) but for radio-burst patterns at 13:35 UT (pattern II). The *white arrows* indicate the locations of the HXR sources A and B.

field extrapolations. Another possibility proposed by Sprangle and Vlahos (1983) is that HXR-producing electrons that precipitate excite intense narrow band electromagnetic waves, which can accelerate type III-producing electrons in open field lines that are not connected to the primary acceleration region. For pattern I, Figure 8a shows, as expected for type IIIs, that the sources at different frequencies are aligned along the same open flux tubes and that the lower the frequency, the further from the flare site is the radio source. On the contrary, for pattern II, the radio sources are roughly aligned along the north–south direction and do not seem to be magnetically connected to each other (Figure 8b). A possible scenario for pattern II is that electrons are injected in distinct flux tubes of very different ambient parameters (temperature, density). Under these conditions (i) the evolution of the velocity distribution of propagating electrons with space and time differs from one flux tube to the other, and (ii) the maximum energy density of plasma waves may occur over a limited range of altitudes of a given flux tube. Consequently, for a given flux tube, radio emission is mostly generated over a limited bandwidth so that a radio burst is predominantly observed at one NRH frequency in that flux tube. This complex scenario is consistent with the fact that type III-like bursts belonging to pattern II do not show a continuous drift toward lower frequencies

(see Section 2.4). It also agrees with the multi-drift structures and type U bursts found on the dynamic spectrum (Figure 1b).

Furthermore, accepting the above scenario, a sudden change of the radio source pattern after 13:34:53 UT could be caused by loop–loop interaction at a new position (the acceleration in RB becomes dominant, see Figure 7) and thus by new magnetic field line connectivity involving new trajectories of electron beams.

4. Conclusions

Multi-wavelength spectral and imaging observations obtained over a wide spectral range (from HXR to radio meter waves) have been used to study electron acceleration and transport during the November 5, 1998 (Hα 1B, GOES M1.5) flare at $\sim$13:34 UT. Such observations allowed us to probe small (a few 10^3 km) and large (a few 10^4 km) magnetic structures, *i.e.*, electron acceleration and transport from the low corona/upper chromosphere to the middle corona. This observational material combined with potential and linear force-free extrapolations of the photospheric magnetic field lead to the following conclusions:

(a) Flare energy release and acceleration of HXR-producing electrons were driven by loop–loop interaction at two low lying null points (RA and RB in Figure 7) of the active region magnetic field where magnetic reconnection is expected. RA and RB appeared as two independent regions of electron acceleration. Moreover, the stepwise (quasi-periodic) character of the event in the time intervals II – IV is reminiscent of flares for which interaction of current-carrying loops (*e.g.*, Tajima *et al.* (1987) or MHD oscillations of flaring loops (*e.g.*, Kundu *et al.*, 2001) have been invoked.

(b) The shape of the electron spectrum inferred from the HXR spectrum, which exhibits a downward knee above $\sim$100 keV, is broadly consistent with the expectations of charge particle orbit calculations in magnetic reconnection models. This suggests that DC field acceleration may be the main process that produces electrons below a few hundreds of keV. As was already noted in former multi-wavelength studies (*e.g.*, Chupp *et al.*, 1993; Trottet *et al.*, 1994, 1998; Raulin *et al.*, 2000), the data show that the characteristics of accelerated electrons (numbers, spectral hardness, break energy) vary with spatial changes of the acceleration sources (from RA to RB at the transition from interval I to II, and with the motion of the HXR source B during interval IV).

(c) Although there is a close similarity between the time profiles of the HXR emission and optically thin microwave radiation, the present data provide clear evidence that microwaves are produced by relativistic electrons, which have a harder spectrum than that of electrons emitting HXR below $\sim$100 keV. This is in line with the findings of Kundu *et al.* (1994). Moreover, for GR

flares, the spectrum of the HXR/GR continuum hardens above a few hundreds of keV and Trottet *et al*. (1998, 2000) have shown that the hardness of the spectrum of electrons producing the >10 MeV GR continuum is consistent with the hardness of the electron spectrum which radiates the centimeter–millimeter emission. However, whether or not this spectral hardening was due to different acceleration processes acting in different energy bands remains an open question. In the present event, the downward knee of the photon spectrum above $\sim$100 keV is consistent with an upper energy cut-off of $\sim$300 keV for HXR-emitting electrons accelerated by, *e.g.*, DC field acceleration. Under these conditions, another process is needed to accelerate relativistic electrons which produce the observed microwave emission and a GR continuum which is too weak to be detected within the BATSE sensitivity.

(d) For the present flare, as well as for numerous other flares, there is a close similarity between the time profiles of the HXR, microwave, and dm/m emissions. This strongly supports the idea that electrons producing HXR and microwaves in the low corona and electrons producing the dm/m radio emission in the middle corona have been drawn from the same accelerator(s) (*e.g.*, Trottet, 2003 and references therein). However, potential as well as linear force-free extrapolations of the photospheric magnetic field did not provide evidence for a direct magnetic connection between the HXR-emitting structures and the dm/m radio sources. Some indirect ways to link HXR- and dm/m-emitting electrons have been qualitatively explored. Nevertheless, similar observations combined with magnetic field calculations have to be obtained and performed for other flares in order to establish whether the present situation is specific to the studied flare or applies to other flares.

Acknowledgements

This work benefited from the data of EIT and MDI on SoHO, of TRACE, of BATSE on CGRO, and of HXT on Yohkoh which were provided through the Solar Data Analysis Center at NASA Goddard Space Flight Center. We acknowledge H. Aurass (Potsdam) for providing detailed data from the Tremsdort radio spectrograph and R.A. Schwartz for his help in analyzing BATSE data. We also thank K.-L. Klein for helpful discussions and comments. The Nançay Radio Observatory is funded by the French Ministry of Education, the CNRS, and the Région Centre. This research was supported by CNRS-CNPq collaborative programs between the LESIA at Paris Observatory and CRAAM at Mackenzie University – São Paulo (CNRS/CNPq 12071 and 16548). We thank an anonymous referee whose comments and suggestions contributed to the improvement and clarification of our work. M.K. acknowledges support from the project AV0Z10030501. The work of Y.Y. was supported by NSFC grants (10225313, 10333030), MSTC grant (G2000078403).

References

Aschwanden, M.J.: 1987, *Solar Phys.* **111**, 113.
Aschwanden, M.J.: 2001, *Space Sci. Rev.* **101**, 179.
Aschwanden, M.J., Benz, A.O., and Schwartz, R.A.: 1993, *Astrophys. J.* **417**, 790.
Aschwanden, M.J., Schwartz, R.A., and Alt, D.M.: 1995, *Astrophys. J.* **447**, 923.
Bastian, T.S., Benz, A.O., and Gary, D.E.: 1998, *Ann. Rev. Astron. Astrophys.* **36**, 131.
Brown, J.C. and Kontar, E.P.: 2005, *Adv. Space Res.* **35**, 1675.
Brown, J.C., MacKinnon, A.L., van den Oord, G.H.J., and Trottet, G.: 1991, *Astron. Astrophys.* **242**, 13.
Chupp, E.L., Trottet, G., Marschhauser, H., Pick, M., Soru-Escaut, I., Rieger, E., and Dunphy, P.P.: 1993, *Astron. Astrophys.* **275**, 602.
Correia, E., Costa, J.E.R., Kaufmann, P., Magun, A., and Herrmann, R.: 1995, *Solar Phys.* **159**, 143.
Crosby, N.B., Aschwanden, M.J., and Dennis, B.R.: 1993, *Solar Phys.* **143**, 275.
Démoulin, P., Hénoux, J.C., Mandrini, C.H., and Priest, E.R.: 1997, *Solar Phys.* **174**, 73.
Dulk, G.A. and Marsh, K.A.: 1982, *Astrophys. J.* **259**, 350.
Dulk, G.A. , Kiplinger, A.L., and Winglee, R.M.: 1992, *Astrophys. J.* **389**, 756.
Dreicer, H.: 1959, *Phys. Rev.* **115**, 238.
Fárník, F., Karlický, M., and Švestka, Z.: 2003, *Solar Phys.* **218**, 183.
Fletcher, L. and Hudson, H.S.: 2002, *Solar Phys.* **210**, 307.
Hanaoka, Y.: 1997, *Solar Phys.* **173**, 319.
Holman, G.D.: 1985, *Astrophys. J.* **293**, 584.
Holman, G.D.: 2003, *Astrophys. J.* **586**, 606.
Huang, G. and Ji, H.: 2005, *Solar Phys.* **229**, 227.
Hurley, K., Niel, M., Talon, R., Estulin, I.V., and Dolidze, V.C.: 1983, *Astrophys. J.* **265**, 1076.
Kane, S.R., Benz, A.O., and Treumann, R.A.: 1982, *Astrophys. J.* **263**, 423.
Kaufmann, P., Strauss, F.M., Opher, R., and Laporte, C.: 1980, *Astron. Astrophys.* **87**, 58.
Kaufmann, P., Trottet, G., Giménez de Castro, C.G., Costa, J.E.R., Raulin, J.-P., Schwartz, R.A., and Magun, A.: 2000, *Solar Phys.* **197**, 361.
Kerdraon, A. and Delouis, J.M.: 1997, *Lecture Notes Phys.* **483**, 192.
Kiplinger, A.L., Dennis, B.R., Emslie, A.G., Frost, K.J., and Orwig, L.E.: 1983, *Astrophys. J.* **265**, L99.
Klein, K.-L. and Trottet, G.: 1984, *Astron. Astrophys.* **141**, 67.
Kosugi, T., Makishima, K., Murakami, T., Sakao, T., Dotani, T., Inda, M., Kai, K., Masuda, S., Nakajima, H., Ogawara, Y., Sawa, M., and Shibasaki, K.: 1991, *Solar Phys.* **136**, 17.
Krucker, S., Hurford, G.J., and Lin, R.L.: 2003, *Astrophys. J.* **595**, L103.
Kundu, M.R., White, S.M., Gopalswamy, N., and Lim, J.: 1994, *Astrophys. J. Suppl. Ser.* **90**, 599.
Kundu, M.R., Grechnev, V.V., Garaimov, V.I., and White, S.M.: 2001, *Astrophys. J.* **563**, 389.
Lin, R.P. and Schwartz, R.A.: 1987, *Astrophys. J.* **312**, 462.
Litvinenko, Y.E.: 1996, *Astrophys. J.* **462**, 997.
Martens, P.C.H.: 1988, *Astrophys. J.* **330**, L131.
Nishio, M., Yaji, K., Nakajima, H., and Sakurai, T.: 1997, *Astrophys. J.* **489**, 976.
Pendleton, G.N., Mallozzi, R.S., Paciesas, W.S., *et al.*: 1996, *Astrophys. J.* **464**, 606.
Priest, E.R. and Forbes, T.: 2000, *Magnetic Reconnection: MHD Theory and Applications*, Cambridge University Press, Cambridge, p. 612.
Qiu, J., Lee, J., Gare, D.E., and Wang, H.: 2002, *Astrophys. J.* **565**, 1335.
Ramaty, R.: 1969, *Astrophys. J.* **158**, 753.
Raoult, A., Pick, M., Dennis, B.R., and Kane, S.R.: 1985, *Astrophys. J.* **299**, 1027.
Raulin, J.-P., Kaufmann, P., Olivieri, R., Correia, E., Makhmutov, V., and Magun, A.: 1998, *Astrophys. J.* **498**, L173.

Raulin, J.-P., Vilmer, N., Trottet, G., Nitta, N., Silva, A.V.R., Kaufmann, P., Correia, E., and Magun, A.: 2000, *Astron. Astrophys.* **355**, 355.
Roberts, B., Edwin, P.M., and Benz, A.O.: 1984, *Astrophys. J.* **279**, 857.
Sakai, J.I. and de Jager, C.: 1996, *Space Sci. Rev.* **77**, 1.
Sprangle, P. and Vlahos, L.: 1983, *Astrophys. J.* **273**, L95.
Stähli, M., Magun, A., and Schanda, E.: 1987, *Solar Phys.* **111**, 181.
Tajima, T., Sakai, J., Nakajima, H., Kosugi, T., Brunel, F., and Kundu, M.R.: 1987, *Astrophys. J.* **321**, 1031.
Trottet, G.: 2003, *Adv. Space Res.* **32**, 2403.
Trottet, G., Pick, M., and Heyvaerts, J.: 1979, *Astron. Astrophys.* **79**, 164.
Trottet, G., Chupp, E.L., Marschhauser, H., Pick, M., Soru-Escaut, I., Rieger, E., and Dunphy, P.P.: 1994, *Astron. Astrophys.* **288**, 647.
Trottet, G., Vilmer, N., Barat, C., Benz, A., Magun, A., Kuznetsov, A., *et al.*: 1998, *Astron. Astrophys.* **334**, 1099.
Trottet, G., Rolli, E., Magun, A., Barat, C., Kuznetsov, A., Sunyaev, R., and Terekhov, O.: 2000, *Astron. Astrophys.* **356**, 1067.
Vilmer, N., Trottet, G., Barat, C., Dezalay, J.P., Talon, R., Sunyaev, R., *et al.*: 1995, *Space Sci. Rev.* **68**, 233.
Wang, T.J, Yan, Y.H., Wang, J.L., Kurokawa, H., and Shibata, K.: 2002, *Astrophys. J.* **572**, 280.
Wood, P. and Neukirch, T.: 2005, *Solar Phys.* **226**, 73.
Yan, Y.H.: 2005, *IAU Symp.* **226**, 277.